

Longitudinal instability of a liquid rim

Gilou Agbaglah, Christophe Josserand, and Stéphane Zaleski

Citation: *Phys. Fluids* **25**, 022103 (2013); doi: 10.1063/1.4789971

View online: <http://dx.doi.org/10.1063/1.4789971>

View Table of Contents: <http://pof.aip.org/resource/1/PHFLE6/v25/i2>

Published by the [American Institute of Physics](#).

Related Articles

Asymmetric Rayleigh-Taylor and double-diffusive fingers in reactive systems
Phys. Fluids **25**, 014103 (2013)

Statistical measurements of scaling and anisotropy of turbulent flows induced by Rayleigh-Taylor instability
Phys. Fluids **25**, 015107 (2013)

Detailed analysis of the vibration induced instability of a liquid film flow
Phys. Fluids **25**, 014101 (2013)

Effect of viscosity and shear flow on the nonlinear two fluid interfacial structures
Phys. Plasmas **19**, 122105 (2012)

Mushy-layer dynamics in micro and hyper gravity
Phys. Fluids **24**, 103305 (2012)

Additional information on Phys. Fluids

Journal Homepage: <http://pof.aip.org/>

Journal Information: http://pof.aip.org/about/about_the_journal

Top downloads: http://pof.aip.org/features/most_downloaded

Information for Authors: <http://pof.aip.org/authors>

ADVERTISEMENT



**Running in Circles Looking
for the Best Science Job?**

Search hundreds of exciting
new jobs each month!

<http://careers.physicstoday.org/jobs>

physicstodayJOBS



Longitudinal instability of a liquid rim

Gilou Agbaglah, Christophe Josserand, and Stéphane Zaleski

*Institut Jean Le Rond D'Alembert, UMR 7190, CNRS & UPMC (Univ. Paris 6) Case 162,
4 place Jussieu, F-75252 Paris Cédex 05, France*

(Received 5 May 2012; accepted 5 January 2013; published online 4 February 2013)

We study the transverse instability of a retracting liquid rim using a long wavelength approximation model and full numerical simulations. We observe that the instability of the rim is driven both by the Rayleigh-Taylor mechanism because of the initial rim acceleration, and by the Rayleigh-Plateau one. The coupling between the rim and the sheet stabilizes the rim at long wavelength. Full numerical simulations are in good agreement with the model and the subsequent break-up of droplets is observed in the numerical simulations when the instability is strong enough. © 2013 American Institute of Physics. [<http://dx.doi.org/10.1063/1.4789971>]

I. INTRODUCTION

The dynamics of liquid sheets is at the heart of many complex multiphase flows. Liquid curtains,¹ atomization,^{2,3} and drop splashing⁴⁻⁶ are important examples of such dynamics. When the liquid sheet is free at one end, as for instance when a liquid film is ruptured^{7,8} and if the film is homogenous, it retracts due to surface forces and rapidly reaches the so-called Taylor-Culick velocity when viscous effects are small (small Ohnesorge numbers, defined below),^{9,10}

$$v_{TC} = \sqrt{\frac{2\gamma}{\rho e}}. \quad (1)$$

Here, γ is the surface tension, ρ is the liquid density, and e is the film thickness. Sometimes the film thickness and its velocity can vary in time because e varies as for instance for drop splashing, leading to more complex retracting dynamics.^{6,11} But, in general, the retracting dynamics leads to the formation of a rim at the free edge that grows in time,¹² while capillary waves can propagate along the film.^{13,14} This retracting liquid rim is usually unstable to longitudinal perturbations.^{1,15-17} In particular, this instability can be observed in drop splashing, where it leads to the formation of small droplets.^{5,11} At least two different mechanisms can be invoked for this instability:¹⁸ first, the Rayleigh-Plateau instability is involved when the rim radius is large compared to the film thickness.¹⁹ Second, since the rim is initially accelerated by the retraction dynamics until it reaches the Taylor-Culick velocity, it is subject to a time-dependent Rayleigh-Taylor (RT) (or Richtmyer-Meshkov) instability which initiates the rim deformation. On the other hand, the growth of the rim as it recedes provides a stabilization process for large time.

The goal of this paper is, therefore, to disentangle these different contributions to the rim dynamics using first a simple model coupling the rim and the sheet for large wavelength perturbations so that viscous effects can be neglected. We show in the linear stability analysis of this model that new terms arise from the coupling between the liquid sheet and the rim through the variation of the radius of the rim. Then, the results will be compared to direct numerical simulations of the two-fluids system where the nonlinear dynamics can be captured until the droplet break up.

II. DYNAMICS OF THE RIM

We consider a planar liquid sheet of constant thickness e moving with a constant and homogenous velocity v_e in the y direction connected to a horizontal (i.e., along the x direction) liquid rim,

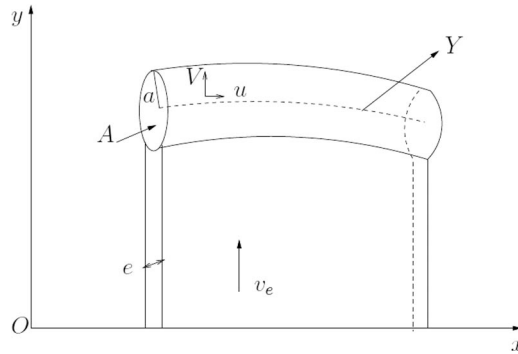


FIG. 1. Spatial configuration of the rim.

supposed to be cylindrical. Assuming that the rim remains close to a straight centerline parallel to the x direction, we will consider long wavelength lateral perturbations (compared to e and the mean rim radius) of the rim. We can then use a two dimensional description of the dynamics using the cartesian coordinate $\{x, y\}$. The rim radius is denoted $a(x, t)$, its cross-section is $A(x, t) = \pi a(x, t)^2$ and the median centerline of the rim is defined by $y = Y(x, t)$, as illustrated on Figure 1. The velocity field inside the rim can be considered in a first approximation depending only on x and t : we introduce then $U(x, t)$ and $V(x, t)$ the velocity fields in the x and y direction, respectively.

In this configuration, the rim dynamics can be described using such a quasi-one-dimensional approach and it is governed by the kinematic condition for the centerline, the mass conservation and the momentum balance equations.^{20,21}

$$\begin{cases} \partial_t Y + U \partial_x Y = V, \\ \partial_t A + \partial_x (UA) = e(v_e - V), \\ \rho A [\partial_t U + U \partial_x U] = -\partial_x (\pi \gamma a - \gamma A \partial_{xx} a) + 2\pi \gamma \partial_x a + 2\gamma \partial_x Y - \rho e (v_e - V) U, \\ \rho A [\partial_t V + U \partial_x V] = 2\pi \gamma \partial_x (a \partial_x Y) - 2\gamma + \rho e (v_e - V)^2, \end{cases} \quad (2)$$

where ρ is the liquid density, while the surrounding gas has been neglected. In contrast to former studies, viscous effects are neglected in our approach.^{16,21,22} In fact, viscous effects would be present directly in the momentum balance in the x and y direction²⁰ and also affect the flow profile inside the rim.²¹ While the direct effect can be neglected in our long wavelength approximation, the Reynolds number associated with the latter effect can be defined as

$$\text{Re} = \frac{\rho \sqrt{\frac{2\gamma}{\rho e}} a_0}{\mu} = \sqrt{\frac{2\gamma \rho e}{\mu^2}} \cdot \frac{a_0}{e},$$

where μ is the dynamical viscosity of the liquid, and a_0 is the typical rim radius. It is related to the inverse of the Ohnesorge number

$$\text{Oh}^{-1} = \sqrt{\frac{2\gamma \rho e}{\mu^2}},$$

multiplied by the aspect ratio a_0/e between the typical rim radius a_0 and the film thickness, which increases in time as the liquid film retracts. The typical inverse of Ohnesorge numbers for 0.1 mm thick water films are of the order of 100. Moreover, the aspect ratios of interest here are larger than 10, so that the viscous effects on the rim can be safely neglected. Inertia from the film and surface tension are the main ingredients of the rim dynamics in Eq. (2) and one of the peculiar properties of retracting film dynamics is that the unperturbed rim retraction (independent of x) is time dependent.¹² To perform the stability analysis of such liquid rim, we will consider that the rim has initially (at time $t = 0$) a constant radius a_i and is subject to an initial acceleration \dot{V}_i , which is

equivalent to consider an initial rim velocity V_i satisfying the relation

$$\rho\pi a_i^2 \dot{V}_i = -2\gamma + \rho e(v_e - V_i)^2.$$

The system of Eq. (2) can be rewritten after rescaling lengths by the initial rim radius a_i and time by

the capillary time $\tau = \sqrt{\frac{\rho a_i^3}{\gamma}}$, following:

$$\bar{x} = \frac{x}{a_i}, \quad \bar{Y}(\bar{x}, \bar{t}) = \frac{Y(x, t)}{a_i}, \quad \bar{t} = \frac{t}{\tau}, \quad (\bar{U}(\bar{x}, \bar{t}), \bar{V}(\bar{x}, \bar{t})) = \left(\frac{U(x, t)\tau}{a_i}, \frac{V(x, t)\tau}{a_i} \right),$$

$$\bar{a}(\bar{x}, \bar{t}) = \frac{a(x, t)}{a_i}, \quad \bar{v}_e = \frac{v_e\tau}{a_i} \quad \text{and} \quad \bar{e} = \frac{e}{a_i}.$$

We then obtain

$$\begin{cases} \partial_{\bar{t}}\bar{Y} + \bar{u}\partial_{\bar{x}}\bar{Y} = \bar{V}, \\ \bar{a}\partial_{\bar{t}}\bar{a} + \frac{1}{2}\bar{a}^2\partial_{\bar{x}}\bar{u} + \bar{u}\bar{a}\partial_{\bar{x}}\bar{a} = \frac{\bar{e}}{2\pi}(\bar{v}_e - \bar{V}), \\ \bar{a}^2\partial_{\bar{t}}\bar{u} + \bar{u}\bar{a}^2\partial_{\bar{x}}\bar{u} = \partial_{\bar{x}}\bar{a} + 2\bar{a}\partial_{\bar{x}}\bar{a}\partial_{\bar{x}\bar{x}}\bar{a} + \bar{a}^2\partial_{\bar{x}\bar{x}\bar{x}}\bar{a} + \frac{2}{\pi}\partial_{\bar{x}}\bar{Y} - \frac{\bar{e}}{\pi}\bar{u}(\bar{v}_e - \bar{V}), \\ \bar{a}^2\partial_{\bar{t}}\bar{V} + \bar{u}\bar{a}^2\partial_{\bar{x}}\bar{V} = 2\bar{a}\partial_{\bar{x}\bar{x}}\bar{Y} + 2\bar{a}^2\partial_{\bar{x}}\bar{a}\partial_{\bar{x}}\bar{Y} - \frac{2}{\pi} + \frac{\bar{e}}{\pi}(\bar{v}_e - \bar{V})^2. \end{cases} \quad (3)$$

In this formulation, it appears clearly that the dynamics are controlled by only two dimensionless parameters, the aspect ratio between the film thickness, the initial rim radius \bar{e} and the initial rim acceleration \dot{V}_i that is set by the initial rim velocity \bar{V}_i , following:

$$\dot{V}_i = -\frac{2}{\pi} + \frac{\bar{e}}{\pi}(\bar{v}_e - \bar{V}_i)^2. \quad (4)$$

Finally, notice that the Taylor-Culick velocity reads in this dimensionless formulation

$$\bar{v}_{TC} = \sqrt{\frac{2}{\bar{e}}}.$$

In the following, we will perform our analysis in this dimensionless framework, omitting the bar in the equations for the sake of simplicity for the reader.

III. SPATIALLY INDEPENDENT SOLUTIONS

Neglecting spatial dependence in the set of Eq. (2), we denote $a_0(t)$, $Y_0(t)$, $U_0(t) = 0$, and $V_0(t)$, as solution of

$$\begin{cases} \dot{Y}_0 = V_0, \\ a_0 \dot{a}_0 = \frac{e}{2\pi}(v_e - V_0), \\ a_0^2 \dot{V}_0 = \frac{e}{\pi}(v_e - V_0)^2 - \frac{2}{\pi}, \end{cases} \quad (5)$$

where \dot{x} denotes the temporal derivative of a variable x .

A second-order ordinary differential equation in terms of the rim radius $a_0(t)$ can be deduced from the system (5),

$$a_0^3 \ddot{a}_0 + 3a_0^2 \dot{a}_0^2 - \frac{e}{\pi^2} = 0. \quad (6)$$

This equation has an analytical solution

$$\pi a_0^2(t) = \sqrt{2et^2 + 2e\pi(v_e - V_i)t + \pi^2},$$

that is, fully determined by the knowledge of the two parameters e and $v_e - V_i$.

From this formula, we observe that, after a quick transient, the rim surface grows linearly in time as expected in the Taylor-Culick regime. In the meantime, the velocity V_0 converges to the Taylor-Culick velocity v_{TC} and the acceleration term \dot{V}_0 rapidly vanishes, so that the system reaches a quasi-stationary regime where only the rim radius increases in time.

IV. LINEAR STABILITY OF A SMALL TRANSVERSE DISTURBANCE

We consider small perturbations to a time dependent homogenous solution (a_0, Y_0, V_0) solution of Eq. (5), in the form

$$\begin{aligned} a(x, t) &= a_0(t) + a_1(x, t), \\ Y(x, t) &= Y_0(t) + Y_1(x, t), \\ U(x, t) &= u_1(x, t), \\ V(x, t) &= V_0(t) + v_1(x, t) \end{aligned}$$

with $|a_1(x, t)| \ll a_0(t)$, $|Y_1(x, t)| \ll a_0(t)$, and $(|u_1(x, t)|, |v_1(x, t)|) \ll v_{TC}$. Replacement of these variables into (3), gives at the first order the linear system

$$\begin{cases} \partial_t Y_1 = v_1, \\ a_0 \partial_t a_1 + a_1 \partial_t a_0 + \frac{1}{2} a_0^2 \partial_x u_1 = -\frac{e}{2\pi} v_1, \\ a_0^2 \partial_t u_1 = \partial_x a_1 + a_0^2 \partial_{xx} a_1 + \frac{2}{\pi} \partial_x Y_1 - \frac{e}{\pi} (v_e - V_0) u_1, \\ a_0^2 \partial_t V_1 + 2a_0 a_1 \partial_t V_0 = 2a_0 \partial_{xx} Y_1 - \frac{2e}{\pi} (v_e - V_0) v_1. \end{cases} \quad (7)$$

Since this system (7) is invariant by translation in the x -direction, we seek Fourier mode solutions: $(Y_1, a_1, u_1, v_1) = (\tilde{Y}_1(t), \tilde{a}_1(t), \tilde{u}_1(t), \tilde{v}_1(t)) \exp(ikx)$, giving

$$\begin{cases} \partial_t \tilde{Y}_1 = \tilde{v}_1, \\ a_0 \partial_t \tilde{a}_1 + \tilde{a}_1 \partial_t a_0 + \frac{1}{2} i k a_0^2 \tilde{u}_1 = -\frac{e}{2\pi} \tilde{v}_1, \\ a_0^2 \partial_t \tilde{u}_1 = i k \tilde{a}_1 - i k^3 a_0^2 \tilde{a}_1 + \frac{2}{\pi} i k \tilde{Y}_1 - \frac{e}{\pi} (v_e - V_0) \tilde{u}_1, \\ a_0^2 \partial_t \tilde{V}_1 + 2a_0 \tilde{a}_1 \partial_t V_0 = -2k^2 a_0 \tilde{Y}_1 - \frac{2e}{\pi} (v_e - V_0) \tilde{v}_1. \end{cases} \quad (8)$$

In this system of equations, we have kept the term $\tilde{a}_1 \partial_t a_0$ in the linear approximation of the mass-conservation equation, by contrast to former approaches.¹⁶ Although this term can be neglected in the large time (large rim) limit, since then $\partial_t a_0 \sim \sqrt{e \cdot v_{TC} / (4\pi t)}$, it can be important for finite-rim radius. The linearized system of Eq. (8) has coefficients that depend on time because the base solution does. Such initial value problems can rarely be solved analytically and usually numerical integration of the system of equations is required. Prior to the study of this general problem, we will consider a regime where the base solution does not evolve rapidly in time compared to the perturbations so that we can assume constant coefficients.

A. Stability analysis with a “frozen” rim

The rim is subject to two phenomena, the growth of its mean radius (described in the base equation (5)) and the evolution of the transverse disturbance. We will consider the so-called frozen rim approximation where we can neglect the temporal evolution of the mean rim radius compared to the linear analysis dynamics. Then, $a_0(t) \sim a_i = 1$ and $\dot{V}_0(t) \sim \dot{V}_i$. We can seek for the solution in the form

$$(\tilde{Y}_1(t), \tilde{a}_1(t), \tilde{u}_1(t), \tilde{v}_1(t)) = (\hat{Y}_1, \hat{a}_1, \hat{u}_1, \hat{v}_1) \exp(\omega t),$$

where ω is the complex growth rate of the transverse perturbation. Within this frozen approximation, the dynamics (8) reduces to the time independent linear system $M \cdot b = 0$, with the matrix

$$M = \begin{pmatrix} \omega & 0 & 0 & -1 \\ 0 & \dot{a}_i + \omega & \frac{1}{2}ik & \frac{e}{2\pi} \\ -\frac{2}{\pi}ik & -ik(1-k^2) & \omega + \frac{e}{\pi}(v_e - V_i) & 0 \\ 2k^2 & 2\dot{V}_i & 0 & \omega + \frac{2e}{\pi}(v_e - V_i) \end{pmatrix}$$

and

$$b = \begin{pmatrix} \hat{Y}_1 \\ \hat{a}_1 \\ \hat{u}_1 \\ \hat{V}_1 \end{pmatrix}.$$

As usual in such linear analysis problems, this equation admits non-trivial solutions only if the matrix M is singular. The determinant of M must be zero and this gives the dimensionless dispersion relation

$$2\omega^4 + 14\dot{a}_i\omega^3 + [28\dot{a}_i^2 + 4k^2 - k^2(1-k^2) - \frac{2}{\pi}e\dot{V}_i]\omega^2 + 4[3\dot{a}_ik^2 + 4\dot{a}_i^3 - \frac{1}{\pi}e\dot{V}_i\dot{a}_i - \dot{a}_ik^2(1-k^2)]\omega + 2k^2[4\dot{a}_i^2 + \frac{2}{\pi}\dot{V}_i - k^2(1-k^2)] = 0. \quad (9)$$

Because of the properties of the base equation (5), we can substitute \dot{a}_i^2 by $\frac{e}{4\pi}(\dot{V}_i + \frac{2}{\pi})$.

This dispersion relation depends therefore only on the two parameters of the problem: the initial acceleration term \dot{V}_i and the dimensionless thickness of the sheet e . Finally, the relation (4) gives the following property: $\dot{V}_i \geq -2/\pi$ with $0 \leq e \leq 1$ since we want to consider only the situation where the rim is always thicker than the liquid film.

In order to understand the influence of these two parameters, we determine for each k the maximum value of the real part ω_r among the four solutions of the dispersion relation, the values of \dot{V}_i and e being fixed. Figure 2 presents the variation of this maximum growth rate for different typical situations. Figure 2(a) where $\dot{V}_i = 0$ shows that the rim growth rate decreases significantly when the dimensionless sheet thickness e increases. This demonstrates the stabilizing role played by the liquid flux entering in the rim by the sheet as illustrated also on Figure 2(b) for $\dot{V}_i = -0.5$. The case $e = 0$ corresponds to the classical infinite cylinder liquid jet instability and the result coincides to the well known Rayleigh-Plateau (RP) classical analysis of the breakup of a liquid jet in the thin thread approximation² (this can be clearly seen by taking $\dot{V}_i = 0$ and $e = 0$ in the dispersion relation). Moreover, one can notice that the most unstable wavenumber remains constant when the dimensionless sheet thickness changes and it is equal to $1/\sqrt{2}$ which correspond to the most unstable wavenumber of the Rayleigh-Plateau instability in the thin thread approximation. The angular point observed in these curves corresponds to the intersection of two different modes and separates two different branches of most unstable mode.

In Figure 2(c), the rim growth rate increases significantly when the acceleration term \dot{V}_i is negative and decreases. Looking at the third equation in (5), the acceleration \dot{V}_i is negative when the capillary forces dominate the inertial forces. Here, the most unstable wavenumber is not constant and depends on the acceleration term \dot{V}_i . Similarly, Figure 2(d) shows that the rim growth rate decreases when \dot{V}_i is positive. These effects are in fact reminiscent of a RT or Richtmyer-Meshkov instability mechanism due to the rim acceleration. Indeed, one can see in the long-wavelength limit $k \rightarrow 0$ and for $e = 0$ that the maximum growth rate of the instability follows $\omega_r \sim (-2\dot{V}_i/\pi)^{1/4}\sqrt{k}$ a dependence in k reminiscent of the RT instability. Indeed, for a pure RT instability of a planar

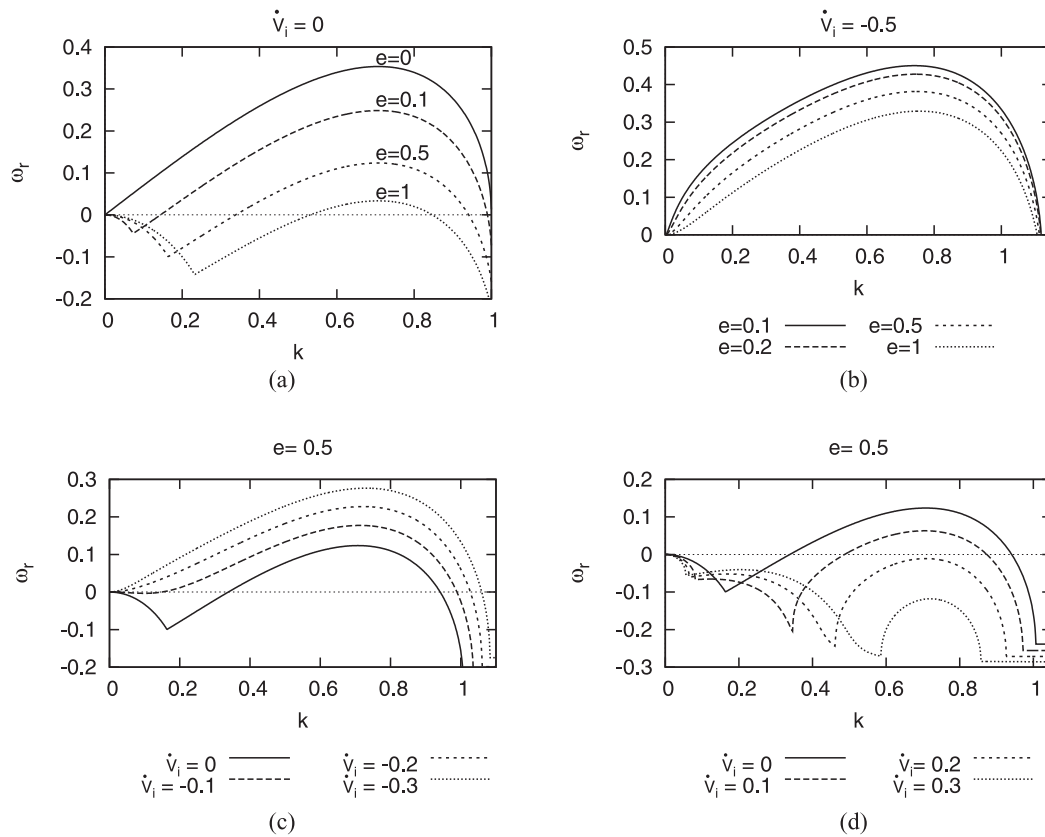


FIG. 2. Growth rate increment in function of the wavenumber in four different cases (a)–(d). The growth rate increases when the thickness of the sheet decreases and when the acceleration term is negative.

instability, one would expect $\omega_r \propto \sqrt{-\dot{V}_i} k$. Here, the power dependence in $-\dot{V}_i$ is different (1/4 instead of 1/2) because the interface (a circle) is curved.

It is interesting to compare these growth rates with recent results obtained in Ref. 16 when viscous effects are included. In particular, in that case, the viscous effects change the structure of the linear system since an additional equation (for the angular momentum) is present. Figure 3 presents a typical comparison between our approach and the viscous theory (called Roisman theory

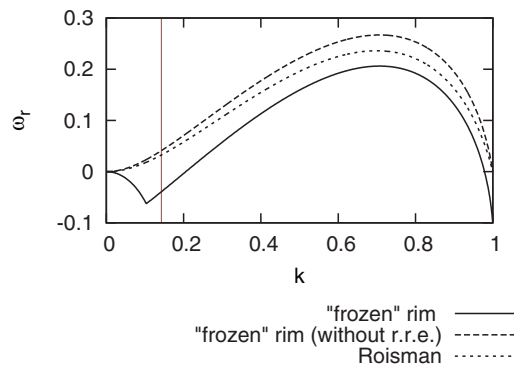


FIG. 3. Comparison between the “frozen” rim solution and Roisman linear theory (2006) for $\bar{e} = 0.2$ and $\dot{V}_i = 0$. “frozen” rim (without r.r.e.): suppressing the “rim radius evolution (denoted by r.r.e.) in the “frozen” rim theory. The vertical line delimits the domain of validity of the linear theory (valid only for $\bar{k} > 0.185$).

later on) for $e = 0.2$ and $\dot{V}_i = 0$. One can immediately notice two important qualitative differences: first, the inviscid theory is apparently always less unstable than the viscous one! In addition, at low wavenumbers, the two approaches exhibit different behaviors. While for the viscous theory the highest growth rate modes are unstable and correspond to the RP instability, the system is, in our approach, linearly stable and the less stable eigenmode has a different structure than that of the RP instability as suggested by the angular point near $\bar{k} \sim 0.15$. These differences are both due to the additional term $\tilde{a}_1 \partial_t a_0$ kept in the linearized system (8) as proven by the long dashed curve on Figure 3, where the growth rates have been recomputed omitting this term. In that case, the highest growth rate modes correspond to the RP instability, similar to the viscous theory, and now the inviscid theory exhibits more unstable modes than the viscous one, as expected. This latter difference is even in good agreement with a viscous attenuation (scaling typically as νk^2) of the modes. Notice that this stabilizing effect at low k is related to the term $\tilde{a}_1 \partial_t a_0$ that decreases as time increases since $\partial_t a_0$ vanishes asymptotically. Therefore, we can conclude first that this term has a strong attenuation effect on the instability at short times only.

However, it is interesting to estimate the validity of the frozen rim approximation by comparing the growth rate of the instability to the typical timescale of the mean radius dynamics. Two limiting cases have to be investigated, depending the initial acceleration of the rim. First, considering the zero acceleration limit, we can compare the radius relative expansion $\partial_t a_0$ with the growth rate of the instability: $\dot{V}_i = 0$, gives the relation $\dot{a}_0^2 = \frac{e}{2\pi^2}$. Since the most unstable situation is obtained for $e = 0$ (as shown in Figure 2) that corresponds to the Rayleigh-Plateau instability, we obtain, using the small k expansion of the Rayleigh-Plateau growth rate: $\omega_{RP} \sim \frac{k}{\sqrt{2}}$,

$$\dot{a}_0 \leq \omega(\leq \omega_{RP}) \Leftrightarrow k > \frac{\sqrt{e}}{\pi}. \quad (10)$$

So that the frozen rim approximation is valid for

$$k > \frac{\sqrt{e}}{\pi}.$$

On the other hand, for the situation where the Rayleigh-Taylor mechanism dominates at small k , one has to compare the RT growth rate $\omega_r \sim (-2 \dot{V}_i / \pi)^{1/4} \sqrt{k}$ with the persistent time of the acceleration $\pi / \sqrt{2e}$, so that taking the highest deceleration of the rim possible ($\dot{V}_i = -2/\pi$) we find that the frozen rim approximation is then valid for

$$k > \frac{e}{\pi}. \quad (11)$$

Since $e < 1$, this second criterion is less restrictive than that computed using the RP instability. Ironically however, one has to notice that the stabilization of the rim dynamics observed for low- k (see, for instance, Figure 3 for $\dot{V}_i = 0$) lies in the region where the frozen rim approximation is not valid anymore! Therefore, the attenuation effect of the term $\tilde{a}_1 \partial_t a_0$ can only be observed for the large enough k , while the stabilization effect at low k will be in general hindered by the time dependent evolution of the unperturbed solution. There a time dependent study is needed to investigate the rim dynamics.

B. Time dependent and nonlinear deformation of the rim

Since the rim radius evolves with time, it is interesting and necessary to characterize the nonlinear and time dependent effects on the perturbed dynamics directly in the framework of this simple model. This can thus be investigated by solving the full nonlinear system of Eq. (3) and it is performed using a Crank-Nicholson scheme with periodic boundary conditions in the horizontal direction. The perturbation of the rim was initialized with a Rayleigh-Plateau mode using the vector

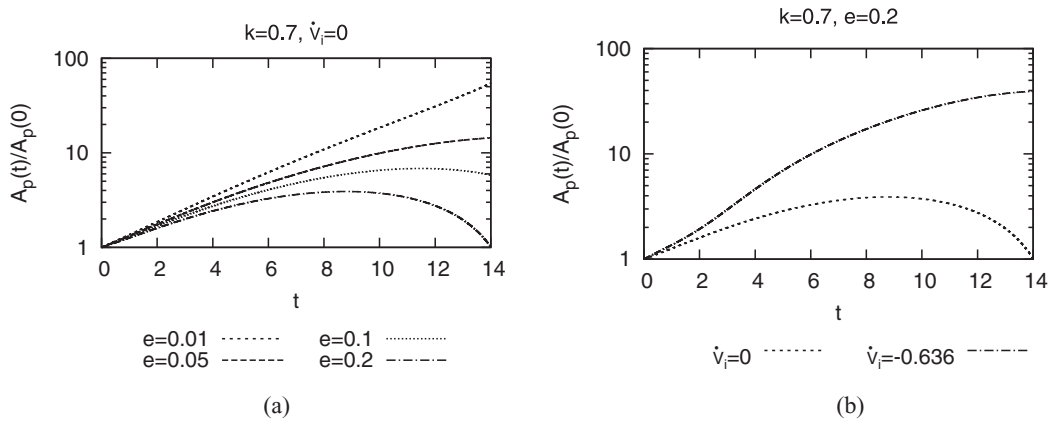


FIG. 4. Time evolution of instability solving the full nonlinear system of Eq. (3) for which the rim radius is time dependent for different aspect ratio e and initial acceleration \dot{V}_i . The linear-log scale shows that the exponential growth is valid only for few time units (a) and (b).

$X(0)$ defined as

$$X(0) = \begin{pmatrix} \tilde{Y}_1(0) = 0 \\ \tilde{a}_1(0) = 1 \\ \tilde{u}_1(0) = 2i \frac{\bar{\omega}}{k} \tilde{a}_1(0) \\ \tilde{V}_1(0) = 0 \end{pmatrix},$$

where $\bar{\omega}$ has been taken from the “frozen”rim analysis.

Figure 4 shows evolution in time (for long times) of the amplitude of the perturbation for different aspect ratios e and initial acceleration \dot{V}_0 , for the same wavenumber $k = 0.7$. We observe an exponential growth for short times in agreement with the frozen rim instability. Then, as expected, the growth of the rim tends to lower the instability growth. Indeed, the larger the film thickness, the stronger is the instability attenuation (see Figure 4(a)), and for the largest aspect ratio we even observe the stabilization of the rim after few time units. Notice that the growth of the amplitude is more than a decade in the zero acceleration limit only for the low film thickness $e \sim 0.01$. On the other hand, moderate values of e can generate a large deformation when the rim is decelerated (see Figure 4(b)), although the growth of the perturbation differs rapidly from an exponential growth.

However, in all these simulations, the dynamics remain in the linear (time dependent) regime, except for the two highest unstable cases where nonlinear dynamics is present. Thus, the main effects on the growth of the perturbations were due to the time dependent dynamics of the rim (radius and acceleration) itself. The overall growth of the perturbations in this framework can be quantified by a so-called amplification factor defined by $\beta(k, t) = \tilde{a}_1(t)/\tilde{a}_1(0)$, which can be computed for every wavenumber k , yielding

$$\beta(k, t) = \exp \left(\int_0^t \text{Re} [\omega(\dot{V}_0(s), e, ka_0(s))] ds \right),$$

where $\text{Re}[\omega(\dot{V}_0(s), e, ka_0(s))]$ is the real part of the growth rate of the mode of wavenumber k . For every mode k , this function β reaches a maximum at some time t_c that depends on k when $\text{Re}[\omega(\dot{V}_0(t_c), e, ka_0(t_c))] = 0$.¹⁵ Consequently, for every time, there exists an optimal mode $k(t)$ which maximizes the amplification of its perturbation. An important question is whether the rim dynamics can eventually enter into a nonlinear stage leading to droplet break-up. Indeed, as demonstrated already in Ref. 15, the linear instability of the rim does not always lead to droplet detachment from the rim because of the growth of rim radius in time, so that every unstable mode eventually becomes linearly stable. Therefore, it could be interesting to perform a parametric study of the function $\beta(k,$

t) for different ratio e and initial acceleration \dot{V}_i in order to determine the optimal mode of the instability for each situation.

Instead of doing this optimal mode determination that we postpone for further studies, we propose in the following a full numerical simulations of the rim dynamics. Beside the advantage of providing a full computation of the dynamics from the linear growth of the perturbations to the droplet break-up, it also allows an alternative test of the linear stability analysis and by consequence of the long wavelength model.

V. FULL NUMERICAL SIMULATIONS

The previous results have been obtained within the long wavelength approximation and the simplified geometry coupling a cylindrical rim with a constant thickness film. It is known that such approximations fail inside the rim where the flow is non-homogenous²¹ and, at the junction between the rim and the film where a neck forms for large enough Reynolds numbers¹⁴ and also when strong linear deformation of the rim occurs, as discussed above. Additionally, the surrounding gas, neglected until now, can also change the interface dynamics. It is thus interesting to compare the results of the model with full three-dimensional (3D) numerical simulations where both the liquid and the gas dynamics are resolved. Such numerical simulations are challenging and rare¹⁵ because of the two large aspect ratios needed (e/a_0 and $k \cdot a_0$) to observe the unstable dynamics until the final stage where droplets detach.

A. Numerical method

We consider two incompressible fluids (liquid and gas) with constant densities ρ_L and ρ_G and constant viscosities μ_L and μ_G , described by the two-fluid Navier-Stokes equations

$$\begin{aligned}\rho(\partial_t \mathbf{u} + \mathbf{u} \cdot \nabla \mathbf{u}) &= -\nabla p + \mu \Delta \mathbf{u} + \gamma \kappa \delta_s \mathbf{n}, \\ \partial_t \rho + \nabla \cdot (\rho \mathbf{u}) &= 0, \\ \nabla \cdot \mathbf{u} &= 0.\end{aligned}$$

In this formulation, the density ρ and viscosity μ are constant in each phase and discontinuous at the interface. The Dirac distribution function δ_s expresses the fact that the surface tension term is concentrated at the interface, κ and \mathbf{n} being the curvature and the normal of the interface, respectively.

Numerical simulations are performed using the GERRIS²³ free code where the interface is tracked using a volume-of-fluid method on a octree structured grid allowing adaptive mesh refinement, while the incompressibility condition is satisfied thanks to a multigrid solver.^{24,25} This numerical code has been validated with numerous examples and has been used successfully, in particular, for many different multiphase problems.^{26,27}

B. Numerical simulation

We take the air/water configurations by setting the density and viscosity ratios to $\rho_L/\rho_G = 850$ and $\mu_L/\mu_G = 50$, respectively. The Ohnesorge number of the simulations is 0.5 and the Reynolds number 10, corresponding roughly to the typical thickness of a soap film (~ 100 nm). The initial mesh is set to $64 \times 64 \times 64$. The dynamical mesh refinement is controlled by three criteria: (1) distance to the interface, (2) curvature of the interface, and (3) vorticity magnitude. The maximum refinement is set on the neck region to $256 \times 256 \times 256$ (see Fig. 5). The numerical simulation is performed in the frame moving at the Taylor-Culick velocity so that the velocity at infinity is constant.

Dirichlet boundary conditions are imposed on the velocity field at the bottom boundary where the gas and the liquid are penetrating. An outlet condition is maintained on the top to simulate the moving reference frame and a periodic condition is imposed on the right and left sides. The problem is solved in dimensionless variables so that the lengths, velocity, and times are in units of the film

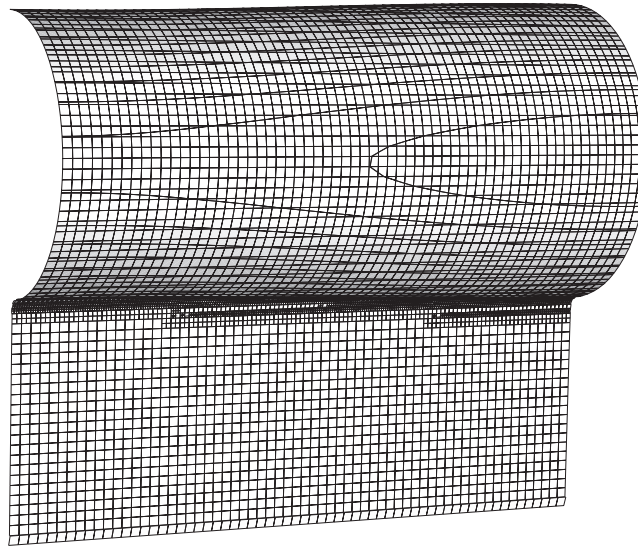


FIG. 5. Initial configuration of the rim and initial mesh. The mesh is refined around the neck wherever the curvature of the interface is large.

thickness e , the Taylor-Culick velocity v_{TC} and capillary time $\tau_n = \sqrt{\rho_L e^3 / \gamma} = (e/a_0)^{3/2} \tau$ (notice the different time units between the analysis and the full numerics).

To avoid numerical film break-up at the rim neck, at least three mesh points are maintained inside the sheet (there the thickness of the sheet corresponds to the physical value of $234.4 \mu\text{m}$). We will use the numerical simulation both to obtain the growth rate of periodic perturbations in order to compare with the results of the linear theory obtained above and also to observe how such perturbations can eventually lead to droplet break-up. The initial shape of the rim is given by its radius: $a(x) = a_0[1 + \epsilon \sin(kx)]$, where ϵ is the amplitude of the perturbation, k its wavenumber ($k = 2\pi/\lambda$, λ being the wavelength), and a_0 is the initial mean radius (in the following, we take $e/a_0 = \bar{e} = 0.2$). The longitudinal velocity field $u(x)$ corresponding to the RP linear mode was also taken for the initial velocity. In order to reduce the computational cost, we make use of two symmetries of the problem: first, only one side of the rim and the film are simulated (planar symmetry of the configuration, see Fig. 5), then we solve the problem on a half-wavelength using the mirror symmetry.

Taking the unperturbed initial solution ($\epsilon = 0$), we observe both the formation of a rim at the free end of the sheet and the neck behind the rim, in good agreement with the base solution described in Sec. III. After a quick transient, this quasi-steady state is reached and the rim velocity tends to zero (in the comoving frame of reference), meaning that the rim reaches the Taylor-Culick velocity. The velocity profile in the median plane inside the sheet is drawn in this steady state on Figure 6: it shows that the velocity inside the rim cannot be considered as constant as in the simplified model above. This was expected because of the velocity difference (v_{TC}) between the film and the rim in this quasi-steady regime. However, we observe that the velocity inside the rim exhibits an exponential decreasing profile starting from the neck so that the velocity is rapidly converging to the constant receding speed. Therefore, to improve numerical accuracy, we will use this velocity profile inside the rim as an initial condition for the zero acceleration case ($\dot{V}_i = 0$). Figure 5 illustrates the initial configuration with the mesh grid on the interface.

C. Results

To investigate the growth rates of the linear modes, we start with an initial amplitude of the perturbation $\epsilon = 0.05$ for different wavenumbers, with $\dot{V}_i = 0$ so that we can use the velocity profile in the rim obtained numerically. We measure the amplitude $A_p(t)$ of the perturbations through the

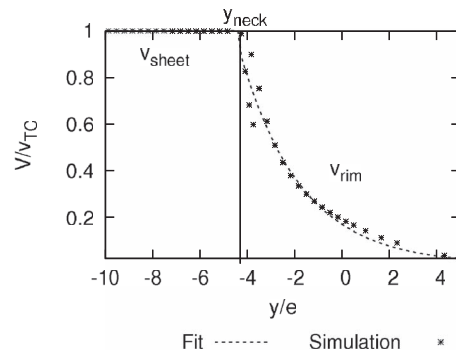


FIG. 6. Velocity profile in the median plane inside the liquid sheet when the steady state is reached. Here, the fit corresponds to: $v_{rim} = 0.1 \exp(-0.39(y - y_{neck}))$, where y_{neck} is the vertical coordinate of the neck, defined as the position of the minimum film thickness.

interface position in the symmetry plane $z = 0$. Figure 7 shows a comparison between the temporal evolution of the amplitude and the “frozen” rim theory for two typical situations. A good agreement is obtained for short times as it is expected since in that configuration we have estimated that the “frozen” rim approximation is valid for $t < 0.4$ in good agreement with previous works¹⁵ (Figure 7(a)). On the other hand, the amplitude of the perturbation decreases very quickly for $k = 0.1$ (Figure 7(b)) and does hardly exhibit an exponential evolution at short times.

The growth rate is then defined as the slope for short times of the function $\log[A_p(t)/A_p(0)]$. Growth rates computed from the full numerical simulations of the dynamics are compared with the linear theory presented above and the viscous linear theory¹⁶ in Figure 8. The agreement is reasonable with both theories, but we would like to emphasize here that the full numerical simulations allow for a discrimination between the two approaches in favor of the inviscid theory developed here (compared to the viscous one).

D. Liquid finger formation

Starting from a linearly unstable configuration, we will try to observe the formation of liquid fingers and eventually droplet break-up from the rim dynamics. Although formally easily to reach, such general dynamics ranging from the linear growth of the perturbations towards the nonlinear fingering and droplet break-up have not been observed yet in full numerical simulation because of the stabilizing effect of the growth of the rim radius. Indeed, it has been argued in Ref. 15 using the Rayleigh-Plateau linear theory that a wavenumber $|k| \leq 2\pi/100$ is needed to obtain an amplification

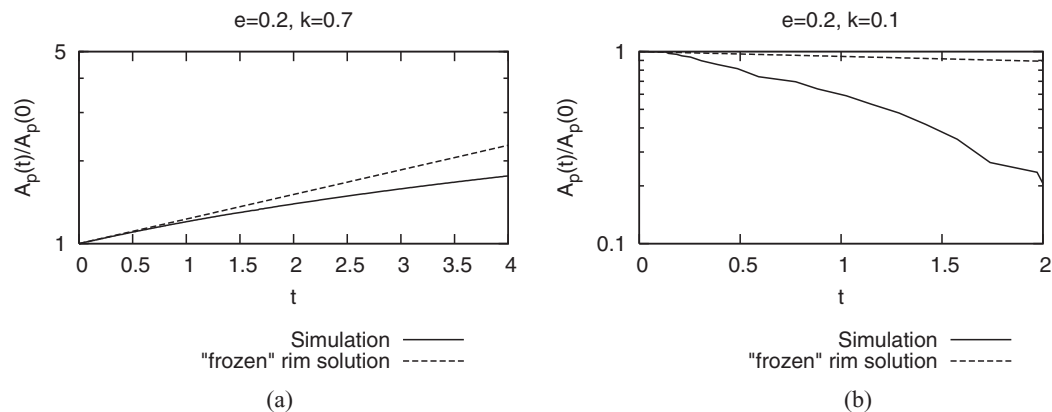


FIG. 7. Comparison of the time evolution of the amplitude of the perturbation and “frozen” rim theory for two different wavenumbers (a) and (b).

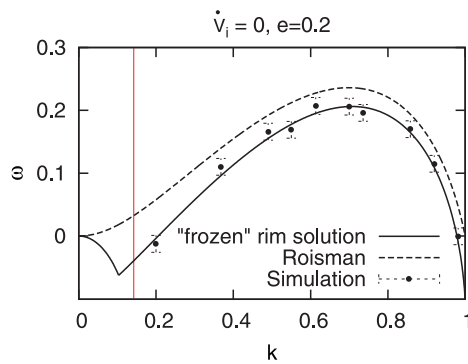


FIG. 8. Comparison between the present theory, the viscous theory,¹⁶ and the results of the full numerical simulation. The vertical line delimits the domain of validity of the linear theory (valid only for $\bar{k} > 0.185$).

factor of 100. Coupled for instance with the aspect ratio used for the above computations $e = 0.2$ and the numerical requirement of three grid points in the film, it gives a minimum aspect ratio between the wavelength and the grid size of 1500 which makes a regular grid 3D computations extremely difficult! Here, we will take advantage of both the mesh refinement technique that allows high aspect ratio without implementing a regular grid and the Rayleigh-Taylor mechanism (through a negative

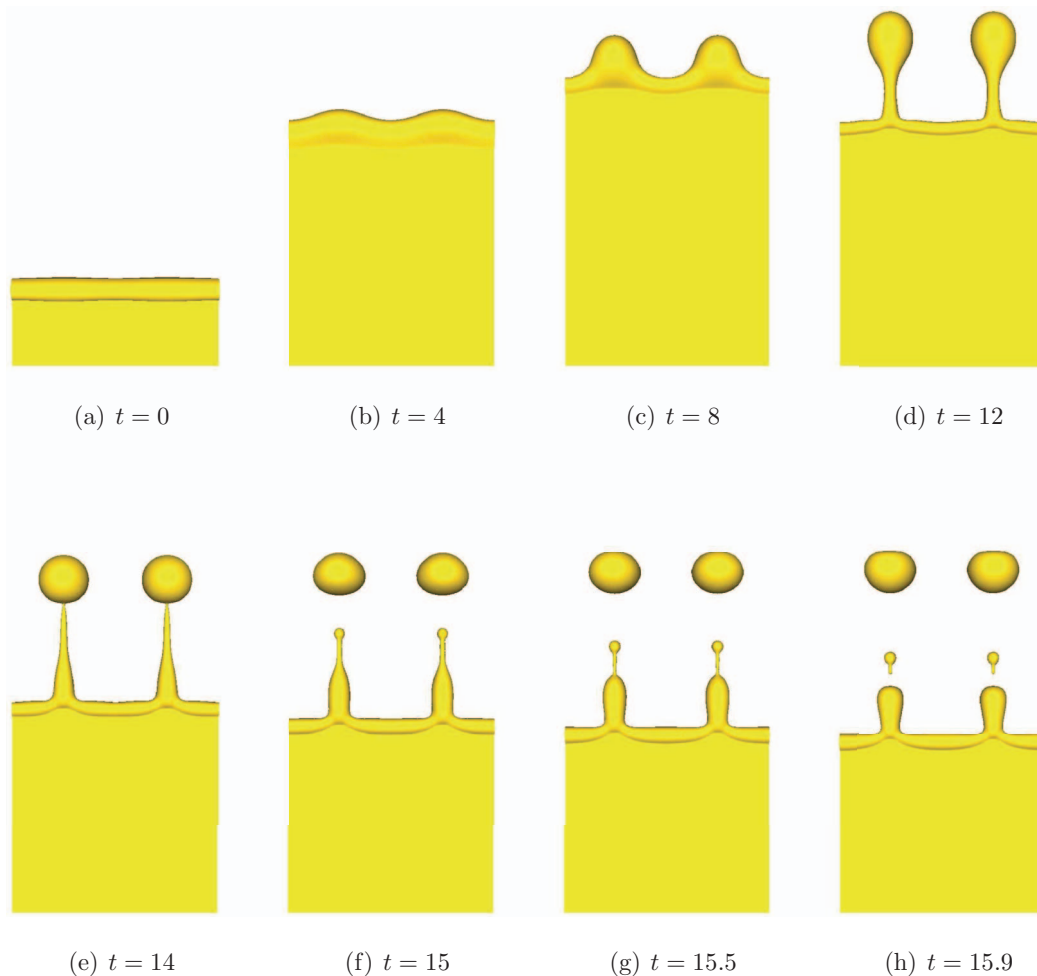


FIG. 9. Liquid finger formation and rim breakup for $el_0 = 0.05$, $\lambda/l_0 = 8.5$, and $\dot{V}_i = -2/\pi$ (a)–(h).

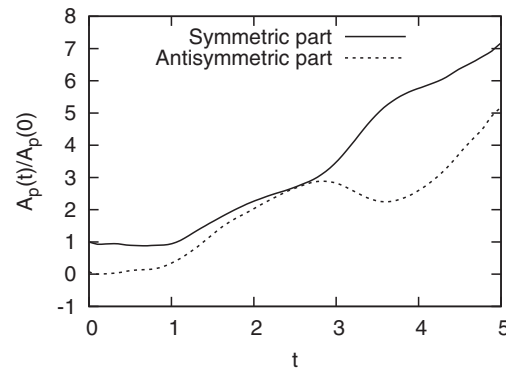


FIG. 10. Relative growth of the symmetrical and antisymmetrical part of the rim instability for the case shown in Figure 9, $\epsilon/a_0 = 0.05$, $\lambda/a_0 = 8.5$, and $V_i = -2/\pi$.

initial value of \dot{V}_i) to numerically reach a situation where fingers and droplet can detach. Indeed, from the system of equations for the base solution (5), we observe that the acceleration \dot{V}_i is negative when $|v_e - V_i| < \sqrt{2/e}$. The largest negative value of \dot{V}_i is obtained for $v_e = V_i$, giving $\dot{V}_i = -2/\pi$. We show in Figure 9 the full dynamics starting from a small rim perturbation ($\epsilon = 0.05$, at $t = 0$) and leading to finger formation and droplet detachment in this case, taking $e = 0.05$, $\dot{V}_i \simeq 0.636$, and $\lambda/a_i = 8.5$. We would like to point out that such numerical simulation was performed using a parallel version of the numerical scheme and took about 3 weeks on 20 processors.

The linear instability regime can be seen between Figures 9(a) and 9(b) ($t = 4$), while at $t = 8$ nonlinear deformations of the rim can be seen. We observe that the original symmetric deformation of the rim has deformed into a sinusoidal form at $t = 4$ because of the RT mechanism that dominates at short times. Then, one can argue that a RP type of deformation arises between $t = 4$ and $t = 8$ through the large deformation of the rim radius. The fingers are already initiated and clearly formed in Figure 9(d) ($t = 12$). There, a thin liquid thread separates the forming droplet from the liquid film. This liquid thread stretches so that a droplet detaches (Figure 9(e) at $t = 14$). Then the liquid finger retracts (Figures 9(f), 9(g), and 9(h) for $t = 15$, 15.5, and 15.9, respectively) because of surface tension, leading to the break-up of small satellite droplets at $t = 15.9$ in Figure 9(h). Finally, one can also observe oscillations of the main drop initiated by the drop release. This drop break-up dynamics is in fact generic and in good qualitative agreement with droplet detachment observed in crown splashes.²⁸

VI. DISCUSSION AND CONCLUSION

The linear stability and nonlinear dynamics of a receding liquid sheet has been investigated theoretically and numerically using both an inviscid long-wavelength model and full numerical simulations of the Navier-Stokes equation. Good qualitative and quantitative agreement is found in the regime where the long-wavelength approximation is valid.

It is interesting to question whether this approach could estimate the relevant mechanism causing the detachment of secondary droplets in drop impacts. Indeed, although having been visualized over more than one century, back to Worthington,²⁹ the corrugation and subsequent spatially periodic fingers formation (e.g., Edgertons²⁸ crown) has not yet received a definite answer. This is especially testified by two seemingly contradictory recent studies: Krechetnikov³⁰ suggest that the RT instability predicts the right number of fingers of the crown, while Deegan *et al.*³¹ claim that it is the Rayleigh-Plateau instability that provides the best quantitative agreement. Although our study does not take into account the curvature of the corolla, we believe that it can clarify this apparent discrepancy. Indeed, we can extract from the full numerical simulation presented in Figure 9 the symmetrical and antisymmetrical part of the perturbation, as shown in Figure 10. Roughly speaking, the symmetrical part, or the so-called varicose mode, would correspond to the RP mechanism, while

the antisymmetrical part (sinusoidal mode) describes the RT instability. The initial conditions are purely symmetrical and we observe first at short times a slight decrease of this contribution while the antisymmetrical part is growing. After few unit times both contributions are of the same order and the symmetric part then increases more rapidly. This figure demonstrates that in that case the RT instability is dominant at short times, while the RP becomes relevant at larger times where the rim starts to generate fingers. Therefore, such decomposition shows that the two instability mechanisms are present in the rim dynamics and it suggests that the RT mechanism is dominant at short time when the rim is decelerated strongly enough, while the RP one becomes more important later. In fact, it is possible to compare the growth of these two mechanisms in the long wavelength limit, taking $\omega_{RP} \sim k/\sqrt{2}$ and $\omega_{RT} \sim (-2 \dot{V}_i / \pi)^{1/4} \sqrt{k}$. It shows that the RT mechanism dominates the RP one for $k > 2\sqrt{-2 \dot{V}_i / \pi}$. Together with the limit due to the growth of the rim, Eq. (11), it gives the following condition for the RT instability to be relevant: $-\dot{V}_i > e/(2\pi)$ which in physical units gives

$$-\dot{V}_i > \frac{\gamma e}{2\pi \rho a_i^3}.$$

Notice that similarly both RT and RP mechanism are present during the drop impact, the RT being important at short times when the splash is rapidly decelerated, while RP becomes relevant at longer time if a corolla has formed. It explains the different features observed by the two previous studies although only qualitative analysis can be performed since we are not able to quantify the important parameter e (the thickness of the corolla divided by the radius of the rim). In Ref. 30, we are in a so-called prompt splash configuration where a rapid jet is formed at short times. In that regime, the dimensionless thickness of the corolla is relatively big $e \sim 1$ and the deceleration is in order of 10^5 m/s^2 . On the other hand, as the size of the rim grows with time, e decreases rapidly and the deceleration of the corolla almost vanishes (see, for instance, Fig. 12 of Ref. 31). In this limit, the rim is subjected to the RP instability which is the conclusion in Ref. 31.

ACKNOWLEDGMENTS

It is our pleasure to thank Stéphane Popinet and Pascal Ray for valuable discussion. Financial support of the *Agence Nationale de la Recherche* through the Grant No. DEFORMATION ANR-09-JCJC-0022-01 is greatly acknowledged.

- ¹L. Limat, P. Jenffer, B. Dagens, E. Touron, M. Fermigier, and J. E. Wesfreid, "Gravitational instabilities of thin liquid layers: Dynamics of pattern selection," *Physica D* **61**, 166 (1992).
- ²J. Eggers and E. Villermaux, "Physics of liquid jets," *Rep. Prog. Phys.* **71**, 036601 (2008).
- ³G. Tomar, D. Fuster, S. Zaleski, and S. Popinet, "Multiscale simulations of primary atomization," *Comput. Fluids* **39**, 1864–1874 (2010).
- ⁴M. Rein, "Phenomena of liquid drop impact on solid and liquid surfaces," *Fluid Dyn. Res.* **12**, 61 (1993).
- ⁵A. L. Yarin and D. A. Weiss, "Impact of drops on solid surfaces: Self-similar capillary waves, and splashing as a new type of kinematic discontinuity," *J. Fluid Mech.* **283**, 141–173 (1995).
- ⁶C. Josserand and S. Zaleski, "Droplet splashing on a thin liquid film," *Phys. Fluids* **15**, 1650 (2003).
- ⁷G. Debrégeas, P. Martin, and F. Brochard-Wyart, "Viscous bursting of suspended films," *Phys. Rev. Lett.* **75**, 3886 (1995).
- ⁸H. Lhuissier and E. Villermaux, "The destabilization of an initially thick liquid sheet edge," *Phys. Fluids* **23**, 091705 (2011).
- ⁹G. I. Taylor, "The dynamics of thin sheets of fluid. II. Waves on fluid sheets," *Proc. R. Soc. London A* **253**, 296–312 (1959).
- ¹⁰F. E. C. Culick, "Comments on a ruptured soap film," *J. Appl. Phys.* **31**, 1128–1129 (1960).
- ¹¹E. Villermaux and B. Bossa, "Drop fragmentation on impact," *J. Fluid Mech.* **668**, 412–435 (2011).
- ¹²J. B. Keller, A. King, and L. Ting, "Blob formation," *Phys. Fluids* **7**, 226 (1995).
- ¹³G. Sinderhauf, H. Raszillier, and F. Durst, "The retraction of the edge of a planar liquid sheet," *Phys. Fluids* **14**, 198 (2002).
- ¹⁴L. Gordillo, G. Agbaglah, L. Duchemin, and C. Josserand, "Asymptotic behavior of a retracting two-dimensional fluid sheet," *Phys. Fluids* **23**, 122101 (2011).
- ¹⁵J. M. Fullana and S. Zaleski, "Stability of a growing end rim in a liquid sheet of uniform thickness," *Phys. Fluids* **11**, 952 (1999).
- ¹⁶I. V. Roisman, K. Horvat, and C. Tropea, "Spray impact: Rim transverse instability initiating fingering and splash, and description of a secondary spray," *Phys. Fluids* **18**, 102104 (2006).
- ¹⁷N. Bremond, C. Clanet, and E. Villermaux, "Atomization of undulating liquid sheets," *J. Fluid Mech.* **585**, 421–456 (2007).

- ¹⁸R. Krechetnikov, "Stability of liquid sheet edges," *Phys. Fluids* **22**, 092101 (2010).
- ¹⁹R. D. Deegan, P. Brunet, and J. Eggers, "Complexities of splashing," *Nonlinearity* **21**, C1 (2008).
- ²⁰A. Oron, S. H. Davis, and S. G. Bankoff, "Long-scale evolution of thin liquid films," *Rev. Mod. Phys.* **69**, 931 (1997).
- ²¹A. L. Yarin, *Free Liquid Jets and Films* (Longman, 1993).
- ²²I. V. Roisman, "On the instability of a free viscous rim," *J. Fluid Mech.* **661**, 206–228 (2010).
- ²³S. Popinet, Gerris flow solver, see <http://gfs.sourceforge.net/>. Gerris is a Free Software program for the solution of the partial differential equations describing fluid flow.
- ²⁴S. Popinet, "Gerris: A tree-based adaptive solver for the incompressible euler equations in complex geometries," *J. Comput. Phys.* **190**(2), 572–600 (2003).
- ²⁵S. Popinet, "An accurate adaptive solver for surface-tension-driven interfacial flows," *J. Comput. Phys.* **228**, 5838–5866 (2009).
- ²⁶D. Fuster, G. Agbaglah, C. Josserand, S. Popinet, and S. Zaleski, "Numerical simulation of droplets, bubbles and waves: State of the art," *Fluid Dyn. Res.* **41**, 065001 (2009).
- ²⁷G. Agbaglah, S. Delaux, D. Fuster, J. Hoepffner, C. Josserand, S. Popinet, P. Ray, R. Scardovelli, and S. Zaleski, "Parallel simulation of multiphase flows using octree adaptivity and the volume-of-fluid method," *C. R. Mec.* **339**, 194–207 (2011).
- ²⁸H. E. Edgerton and J. R. Killian, *Flash* (Branford, Boston, 1954).
- ²⁹A. M. Worthington, "On the spontaneous segmentation of a liquid annulus," *Proc. Phys. Soc. London* **30**, 49 (1879).
- ³⁰R. Krechetnikov, "Crown-forming instability phenomena in the drop splash problem," *J. Colloid Interface Sci.* **331**, 555–559 (2009).
- ³¹L. V. Zhang, P. Brunet, J. Eggers, and R. D. Deegan, "Wavelength selection in the crown splash," *Phys. Fluids* **22**, 122105 (2010).